A Hybrid Framework for Porosity Estimation and Property Prediction in Fused Deposition Modeling Parts: Mechanical Analysis

Mahmood Jafari, Heshmat Mohammadkhanloo *, Ali Nouri

[1] Aerospace Engineering Department, Shahid Sattari Aeronautical University of Science and Technology, Tehran, Iran

ORCID: Mahmood Jafari: https://orcid.org/0009-0009-2029-5866

ORCID: Heshmat Mohammadkhanloo: https://orcid.org/0009-0005-4621-2652

ORCID: Ali Nouri: https://orcid.org/0000-0002-2080-6306

***** Corresponding author's email: h_khanloo@ssau.ac.ir

Abstract

Fused Deposition Modeling inherently induces inter-raster voids, which act as stress concentrators and significantly compromise the mechanical and dynamic integrity of printed components. This research presents a novel hybrid framework that integrates semi-empirical characterization with analytical modeling to quantify porosity and predict its effect on the modal behavior of Polylactic Acid beams. Moving beyond simplified circular approximations, a data-driven geometric model employing the Superellipse function was developed to map the actual void morphology based on Scanning Electron Microscopy and G-code toolpaths. These quantitative porosity estimates were subsequently incorporated into a stiffness-reduction constitutive model within the context of Classical Laminate Theory. Experimental validation, utilizing Digital Image Correlation and modal analysis, confirmed the model's accuracy (porosity range: 1.3%–1.9%). Crucially, the findings reveal a direction-dependent frequency response: while the 0° raster angle maintains relative frequency stability due to a balanced reduction in mass and stiffness, the 90° raster angle exhibits a disproportionate stiffness decay, resulting in a precipitous drop in natural frequencies (up to 27%). This study establishes porosity not merely as a defect, but as a critical design parameter for predicting the dynamic performance of Fused Deposition Modeling structures.

Keywords: Fused Deposition Modeling, Void, Superellipse Function, Mechanical and Modal Testing

1. Introduction

Additive manufacturing (AM), especially when using Fused Deposition Modeling (FDM), has become a basic production technology in many different industries because it allows the creation of complex shapes [1-3]. The layer-by-layer extrusion process involved in this method leads to incomplete fusion between neighbouring polymer filaments, so that inter-raster voids are inevitable [1, 4, 5]. Instead of being merely random defects caused by the printing process, these voids are a key characteristic of the final microstructure. Since they act as stress concentrators and decrease the effective cross-sectional area, they greatly impair the load-bearing capacity, structural integrity, and dynamic performance of the printed parts [3-6].

In order to understand, model, and reduce the effect of porosity on the performance of 3D-printed components, researchers have employed a range of analytical and computational methods [7, 8]. The early analytical work made heavy use of linear homogenization theories and simple models such as the rule of mixtures and Classical Laminate Theory (CLT), which assumed that the shapes of the voids were ideal circles or rectangular areas [8-10]. Since these strict geometric assumptions did not take into account the real stress concentrations at the corners, they greatly miscalculated the structural stiffness and underestimated the deterioration of the transverse and shear elastic properties [7, 11]. In order to overcome these limitations, researchers have developed more sophisticated closed-form analytical models based on conformal mapping in

ACCEPTED MANUSCRIPT

elasticity theory [12]. However, their idealised configurations—such as perfect circles, rectangles, or shapes with infinitely sharp corners—still have difficulty in accurately representing actual deformations, flattening effects [8], and the true curvature of the filaments caused by melt flow and viscous sintering before solidification [5]. On the computational side, the use of finite element method (FEM) simulations with elliptical geometries and direct modelling of the microstructure has greatly improved the accuracy of predictions regarding failure and tensile behaviour, even though this comes with very high computational costs [7, 11]. Although the recent increase in advanced imaging techniques such as X-ray computed tomography (XCT) has allowed for the exact three-dimensional analysis of pore dimensions, spatial distributions, and volume fractions [13, 14], there remains a difficulty in turning this empirical data into practical models. This is because XCT outputs are non-parametric voxel volumes and so cannot be directly used in closed-form analytical constitutive equations; furthermore, regular 3D volumetric scanning is still obstructed by major economic and logistical difficulties for use in ordinary design optimization and engineering procedures [11, 14].

In order to overcome these limitations, the Superellipse function provides a flexible mathematical approach. Unlike traditional models, which depend on strict geometric assumptions (for example, perfect circles or rectangles), its variable roundness factor is able to accurately represent both the flattening effect of the molten polymer and the finite curvature of the void corners at the same time. Thus, it gets rid of the stiffness estimation errors that were present in the earlier idealized models and fits smoothly into the macroscopic equations of analytical mechanics. Even though a great deal of work has already been carried out on the parametric analysis of the elastic constants and the static behaviour of FDM-produced structures, studies concerning their dynamic properties—especially the way that the manufacturing microstructures affect natural frequencies—have still been largely neglected and constitute a major gap in the existing literature [15]. Finally, developing a quantitative, accurate understanding of how this realistic void morphology affects the vibrational behavior of 3D-printed parts is essential to avoid resonance phenomena and ensure overall structural safety.

This study presents a combined semi-empirical and computational method for estimating porosity and assessing its effect on the mechanical and dynamic properties of FDM-printed Polylactic Acid (PLA) components. Unlike the simplified geometries that have typically been assumed in previous research, we determined the exact morphology of the inter-filament voids by applying an orthogonal distance regression (ODR) method to fit a parametric super-ellipse function to the Scanning Electron Microscopy (SEM) cross-sectional images and then combining this with the real G-code toolpaths. The geometric parameters obtained in this way were then used in a stiffness-reduction structural model—which was based on CLT and the Euler-Bernoulli beam theory—to predict the structure's macroscopic mechanical behaviour and natural frequencies. The results were verified using Digital Image Correlation (DIC) and experimental modal analysis, showing that the proposed parametric approach offers a reliable and highly accessible means of predicting the performance of 3D-printed parts in practical engineering applications.

2. Materials and methods

2.1. Introducing the FDM method and inter-raster void

FDM is an additive manufacturing method that builds objects by laying down layers of melted thermoplastic material. Each layer consists of thin strands, called rasters, placed next to each other. This way of depositing material leaves small gaps, known as inter-raster voids, between the strands. As more layers are added from the bottom up, they stick together through heat, forming a structure with different properties in different directions. Fig. 1 shows how the FDM process works and where these voids form.

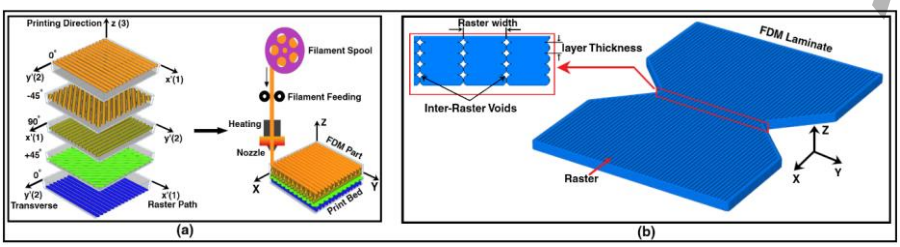


Fig. 1 (**a**) FDM: layer-by-layer fabrication, (**b**) FDM part with voids

ACCEPTED MANUSCRIPT

2.2. Material and Specimen Fabrication

Standard tensile (ASTM D638 Type I), shear (ASTM D7078), and beam specimens (280×40×4 mm) were initially sliced using Simplify 3D software. Slicing was performed at raster angles of 0°, 90°, and ± 45° symmetrically, according to the parameters specified in Table 1 (Fig. 2a and 2b). The specimens were then fabricated using a 3D printer with a build volume of 360×360×360 mm.

Table 1 FDM process parameters for fabrication of parts

Parameters	Values
Filament Diameter (mm)	1.75
Filament Density (kg/m^3)	1250
Nozzle Diameter (mm)	0.4
Layer Height (mm)	0.1
Infill Percentage (%)	100
Raster Angle	[0°], $[\pm 45^\circ]_s$, [90°]
Nozzle Temperature (°C)	220
Heat Bed (°C)	60
Printing Speed (mm/s)	80

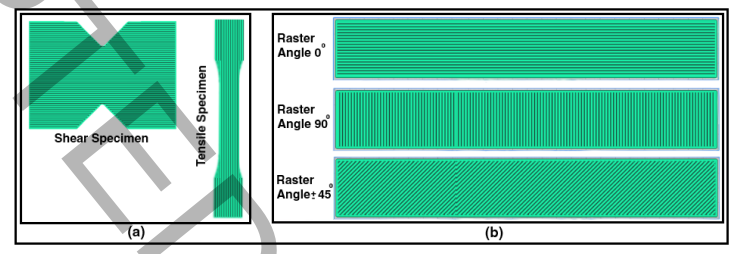


Fig. 2 (a) Standard specimens, (b) FDM beam with different raster angles

2.3. Micro-structural Analysis of FDM 3D Printing

Analysis of the SEM images in Fig. 3 provides insight into the internal structure of the PLA sample, produced via FDM using the settings in Table 1. The images show gaps between printed lines (rasters), often appearing as triangles or diamonds. These gaps, called inter-raster void, result from incomplete bonding of semi-melted plastic rasters during printing.

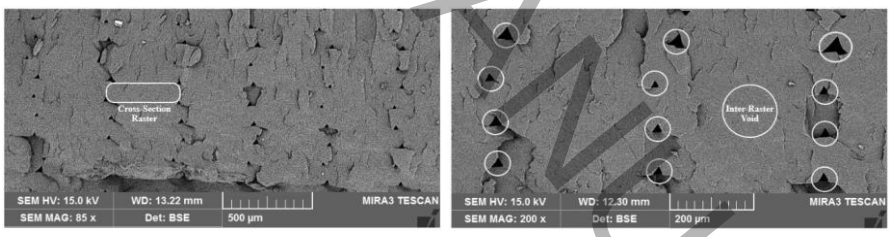


Fig. 3 Micro-structure of FDM 3D printing part

2.4. Semi-Experimental Method for Porosity Estimation

This study introduces a new semi-empirical computational framework aimed at accurately estimating inter-raster porosity. The model connects the cross-sectional geometry of printed rasters to the precise G-code toolpaths generated by Simplify-3D slicer software, using optimized curve fitting on points obtained from SEM images.

The development and implementation stages of this model are as follows:

1. Microstructure Analysis and Geometric Model Selection: The analysis of the microstructure and the choice of geometric model show that the cross-sections obtained by printing are not ideal but instead have the shape of elongated rectangles with rounded corners because of the high ratio of nozzle diameter to layer height [16]. In order to reduce the errors caused by circular approximations, the Superellipse function was used.
2. Geometric Modeling: The Superellipse mathematically represents this geometry (Fig. 4) via the following implicit equation:

$$|x/a|^n + |y/b|^n = 1 \quad (1)$$

ACCEPTED MANUSCRIPT

In this case, *a* denotes the half-width, *b* the half-height, and *n* is the roundness factor. The main benefit of the superellipse as compared to conventional models is the presence of this adjustable *n* parameter, since it allows the model to adapt independently to the actual morphological transitions and thus accurately capture the precise boundary shapes which the earlier fixed-geometry models had not been able to represent.

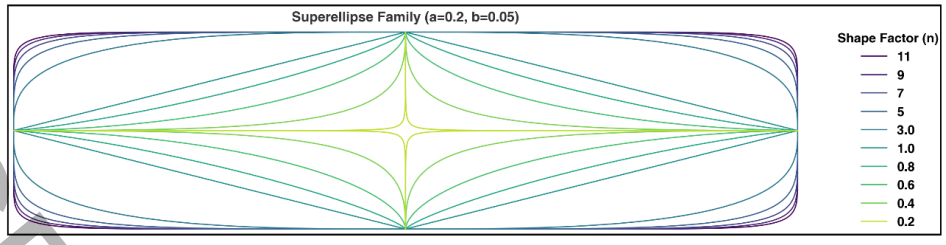


Fig. 4 Superellipse curves

3. Model parameter determination by curve fitting: To accurately represent the cross-sectional shapes of printed strands, the three parameters identified in Step 2 were derived directly from experimental SEM data. This approach accounts for physical effects such as layer flattening and raster stretching (Fig. 5a

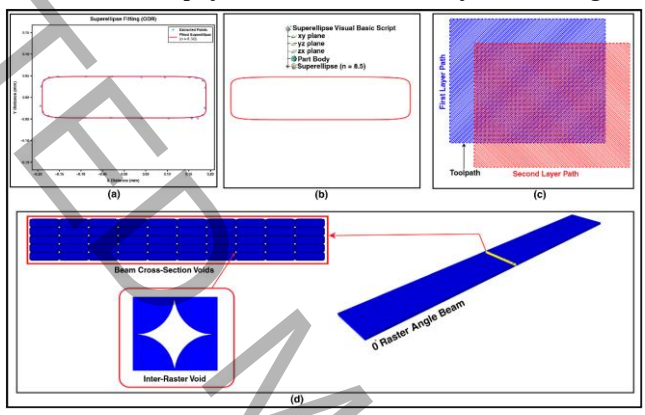


Fig. 5 (**a**) Curve fitting, (**b**) Superellipse VBA script, (**c**) Nozzle toolpath, and (**d**) 3D void modeling

This study used ODR for curve fitting. ODR accounts for measurement errors in both the *x* and *y* axes, which represent raster width and print layer height, respectively. It finds the model parameters by minimizing the squared perpendicular distances between each data point and the curve. The implicit equation that defines the superellipse within the geometric model of the cross-section raster is as follows:

$$f(x, y; \beta) = |x/a|^n + |y/b|^n - 1 = 0 \tag{2}$$

Here, $\beta = (a, b, n)^T$ denotes the model parameter vector. The minimization problem for the objective function *S*, described below, was solved using the SciPy library in Python to estimate the model parameters.

$$\min_{\beta, \{\hat{x}_i, \hat{y}_i\}} \rightarrow S_{ODR} = \sum_{i=1}^{N} \left[w_{x_i} (x_i - \hat{x}_i)^2 + w_{y_i} (y_i - \hat{y}_i)^2 \right]$$
$$\text{Subject to:} \quad f(\hat{x}_i, \hat{y}_i; \beta) = 0 \quad \text{for } i = 1, \ldots, N \tag{3}$$

N represents the total number of experimental data points. The coordinates, (x_i, y_i) denote the raster's edge points extracted from SEM image processing, which serve as the observed data. In contrast, $(\hat{x}_i, \hat{y}_i)$ represent the corresponding coordinates on the ideal superellipse curve. The weights w_{x_i} and w_{y_i} indicate the SEM measurement accuracy in the horizontal and vertical directions, respectively, and are generally assumed to be equal. The parameter *n*, known as the roundness exponent, quantifies the degree of corner rounding in the superellipse. To eliminate algorithmic sensitivity to initial parameter guesses and avoid local minima, the Python solver automatically initializes the half-width (*a*) and half-height (*b*) using the geometric bounding box of each detected void, with an initial roundness conservatively set to *n* = 2. This data-driven initialization ensures highly robust and stable convergence for the ODR model.

ACCEPTED MANUSCRIPT

4. 2D Modeling: A Visual Basic Script (VBScript) is developed in CATIA V5 to import and generate the raster geometry from Step 3 (Fig. 5b), as well as the precise toolpath (G-code) generated by Simplify 3D software (Fig. 5c).
5. 3D Model Generation: The 3D solid model of the part is generated by simulating the nozzle tool path using geometry derived from the superellipse equation. This approach enables adjacent rasters to fit together, resulting in inter-raster voids with more realistic shapes, as illustrated in Fig. 5d.
6. Calculation of porosity percentage: The porosity percentage (p) for each specimen was determined using area measurements obtained from the 3D computational model generated in Step 5, according to the following equation:

$$\text{Porosity}(\%)=\left(\frac{\text{Total area of voids}}{\text{Total area of cross-sectional beads}}\right)\times 100 \tag{4}$$

The porosity estimation model was evaluated by determining the volume fraction of voids using ImageJ software on four SEM images from the gauge section of the ASTM D638-Type I specimen, as shown in Fig. 6. This analysis yielded an average porosity of 1.322 %, a 7 % discrepancy from the model's estimate in Table 2.

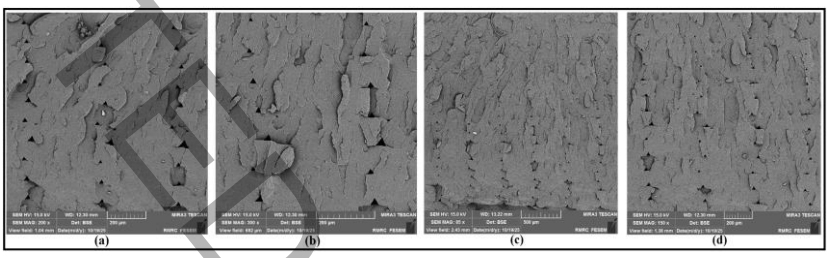


Fig. 6 Cross-section of rasters with porosity values of (p): (**a**) 1.174, (**b**) 1.138, (**c**) 1.338, and (**d**) 1.638

Table 2 Porosity estimation of FDM components via presented method

Part Name	Total area of voids (mm^2)	Total area of cross-sectional rasters (mm^2)	Porosity (%)
ASTM D638-Type I	0.4647	37.6512	1.234
Beam - 0° Raster	2.9920	159.960	87.10
Beam - 90° Raster	22.533	1176.60	1.915
Beam - ± 45° Raster	25.852	1333.48	1.938

2.5. Micromechanical-Structural Formulation for FDM Beams

2.5.1. Porosity-Dependent Effective Properties

Within this analytical framework, the FDM structure is represented as a composite laminate, where each layer demonstrates orthotropic behavior. The structural properties of each layer are defined as functions of the porosity volume fraction (p) and the microscopic geometry of the voids. The effective density is determined using the linear rule of mixtures (Eq. (5)) [5]. In contrast, the longitudinal elastic modulus is evaluated using a nonlinear power-law model (Eq. (6)) [17], which more accurately captures the reduction in stiffness resulting from inadequate interlayer bonding. The transverse and shear moduli are obtained through micromechanical relations based on conformal mapping (Eqs. (7) and (8)), which incorporate the effects of stress concentration due to void geometry [18].

$$\rho_{eff} = \rho_{base}(1-p) \tag{5}$$

$$E_1 = E_{base}(1-p)^m \tag{6}$$

The empirical stiffness-reduction exponent ($m>1$) in Eq. (6) was calibrated using axial tensile data from 0° raster angle samples (1.8–1.9 % porosity). A Python-based nonlinear least-squares optimization fit the model to the data, yielding an optimal $m=1.35$, refining the conservative literature value of $m=2$. It should be noted that this calibrated exponent is specific to the evaluated narrow porosity range, representing high-density prints, and requires further validation before being extrapolated to highly porous components.

ACCEPTED MANUSCRIPT

$$E_2 = E_{base}\left[\frac{1-2c^2}{2pc^2+3p-2c^2+1}\right] \tag{7}$$

$$G_{12} = G_{base}\left[\frac{1-2c^2}{2p-2c^2+1}\right] \tag{8}$$

In these expressions, ρ_{base}, E_{base}, and G_{base} represent the base density, elastic modulus, and shear modulus of the material, respectively, where $G_{base} = E_{base} / 2(1+\nu_{base})$, and c is the geometric parameter that characterizes the void shape. The major Poisson's ratio is assumed to be independent of porosity ($\nu_{12} = \nu$).

2.5.2. Mathematical modeling of void geometry

In contrast to conventional micromechanical modeling approaches [12], which typically assume idealized pore geometries such as perfect circles or triangles with sharp corners (Fig. 7a), this study adopts a data-driven methodology to maximize consistency with the actual fabricated samples. Instead of relying on theoretical default values, the boundary coordinates of the pores were extracted from SEM image processing (Fig. 7b). The hypotrochoidal conformal mapping function (Eq. (9)) [19, 20] was then selected as the baseline mathematical model to fit the experimental data and determine the optimal shape parameter ($\square$):

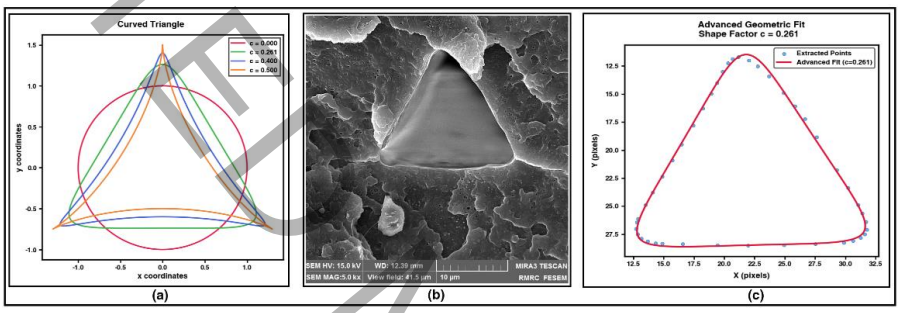


Fig. 7 (**a**) Idealized curved triangles, (**b**) SEM image of void, and (**c**) Mathematical model fitting

$$z(\theta) = R(e^{i\theta} + ce^{-2i\theta})e^{i\alpha} + z_0 \tag{9}$$

In this context, R denotes the scaling factor, alpha specifies the cavity rotation angle, z_0 indicates the center coordinates, and $\square$ determines the sharpness of the shape. The most precise value for the shape parameter (c) was determined by implementing a non-linear least squares optimization algorithm in Python. The objective function minimized the Euclidean error between points extracted from the SEM image and the mathematical model curve. The fitting results (Fig. 7c) identified an optimal value of $c = 0.261$. This experimental result indicates that the commonly assumed value of $c = 0.5$, which represents sharp corners in prior studies, does not accurately reflect the observed geometry and may lead to erroneous estimates of the compliance matrix. Therefore, the experimentally determined value of $c = 0.261$ was used in all subsequent analyses to enhance the accuracy of the results.

2.5.3. Derivation of Stiffness Matrices and Engineering Constants

The micromechanical properties of the layers are first determined, after which the reduced stiffness matrix [**Q**] for each layer is calculated in the principal coordinate system (1-2), as shown in Fig. 8a and according to Eqs. (10) below.

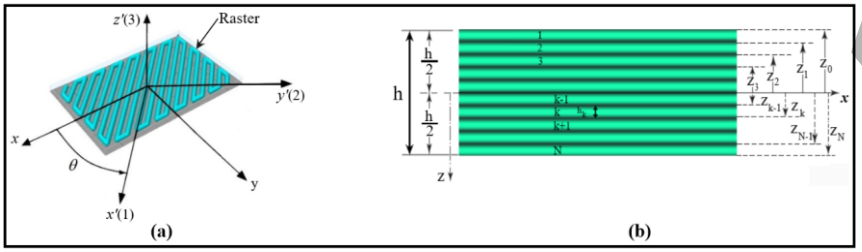


Fig. 8 (**a**) Principal material and geometric coordinates, (**b**) Layer distance from FDM lamination mid-plane

ACCEPTED MANUSCRIPT

$$Q_{11} = \frac{E_1}{1-\nu_{12}\nu_{21}}, \quad Q_{22} = \frac{E_2}{1-\nu_{12}\nu_{21}}, \quad Q_{12} = \frac{\nu_{12}E_2}{1-\nu_{12}\nu_{21}}, \quad Q_{66} = G_{12} \tag{10}$$

The symmetry relation $\nu_{21} = \nu_{12}(E_2 / E_1)$ is satisfied. When layers are oriented at an angle theta with respect to the beam reference axis, the transformed stiffness matrix $[\bar{\mathbf{Q}}]$ is calculated using the transformation matrix $[\mathbf{T}]$ as follows:

$$[\bar{\mathbf{Q}}] = [\mathbf{T}]^{-1}[\mathbf{Q}][\mathbf{T}]^{-T} \tag{11}$$

The extensional $[\mathbf{A}]$, coupling $[\mathbf{B}]$, and bending $[\mathbf{D}]$ stiffness matrices for the entire laminate, which consists of N layers with a total thickness h (Fig. 8b), are subsequently calculated using Eqs. (12) below.

$$(A_{ij}, B_{ij}, D_{ij}) = \int_{-h/2}^{h/2} \bar{Q}_{ij}(1, z, z^2)dz = \sum_{k=1}^{N} (\bar{Q}_{ij})_k \left((z_k - z_{k-1}), \frac{1}{2}(z_k^2 - z_{k-1}^2), \frac{1}{3}(z_k^3 - z_{k-1}^3) \right) \tag{12}$$

These integrations ensure that the influence of microstructural defects, such as porosity, is distributed across all components of the overall structural stiffness. Therefore, to analyze macroscopic behavior and determine the effective tensile and shear moduli in the global coordinate system $(x-y)$, the membrane compliance matrix $[\mathbf{A}^*]$ is utilized. This matrix, defined as the inverse of the tensile stiffness matrix, serves as a connection between the micromechanical behavior of voids and the macroscopic structural response, as detailed below:

$$[\mathbf{A}^*] = [\mathbf{A}]^{-1} = \begin{bmatrix} A_{11}^* & A_{12}^* & A_{16}^* \\ A_{12}^* & A_{22}^* & A_{26}^* \\ A_{16}^* & A_{26}^* & A_{66}^* \end{bmatrix} \tag{13}$$

The effective engineering constants of the laminate, specifically the longitudinal Young's modulus (E_x), the transverse Young's modulus (E_y), and the shear modulus (G_{xy}), are determined as follows:

$$E_x = \frac{1}{hA_{11}^*}, \quad E_y = \frac{1}{hA_{22}^*}, \quad G_{xy} = \frac{1}{hA_{66}^*} \tag{14}$$

2.5.4. Free Vibration Analysis

The classical Euler-Bernoulli model was utilized to analyze beam vibrations [21]. In narrow FDM beams, especially those with asymmetric angle-ply layups (raster angle ± 45°), transverse moments are negligible ($M_y \approx 0$), and the beam exhibits transverse curvature due to the Poisson effect. Furthermore, non-zero bending-twisting couplings (D_{16}, D_{26}) significantly reduce the natural frequencies.

The moment-curvature constitutive relation is reformulated using the flexural flexibility matrix $[\mathbf{D}^*]$ to account for these effects, as follows:

$$\begin{Bmatrix} \kappa_x \\ \kappa_y \\ \kappa_{xy} \end{Bmatrix} = [\mathbf{D}]^{-1} \begin{Bmatrix} M_x \\ M_y \\ M_{xy} \end{Bmatrix} = [\mathbf{D}^*] \begin{Bmatrix} M_x \\ 0 \\ 0 \end{Bmatrix} \tag{15}$$

Here, $[\mathbf{D}^*]$ denotes the inverse of $[\mathbf{D}]$. Therefore, the effective flexural stiffness of the beam, EI_{eff}, is proportional to the beam width, b, and to the reciprocal of the first entry of the compliance matrix, as shown below:

$$EI_{eff} = \frac{b}{D_{11}^*} = b\left(\frac{\det([\mathbf{D}])}{D_{22}D_{66} - D_{26}^2} \right) \tag{16}$$

ACCEPTED MANUSCRIPT

By utilizing the inverse matrix element D_{11}, the model explicitly quantifies and incorporates the structural softening caused by the bending-twisting couplings (D_{16} and D_{26}), ensuring that the anisotropic effects of angle-ply layups are accurately represented in the flexural stiffness.

Substituting this stiffness into the differential equation for free vibration of the beam gives:

$$\frac{b}{D_{11}^*}\frac{\partial^4 w(x,t)}{\partial x^4}+(\rho_{eff}A)\frac{\partial^2 w(x,t)}{\partial t^2}=0 \tag{17}$$

Applying the separation of variables method and solving the characteristic equation for free-free boundary conditions yields the natural frequency of the n-th mode (ω_n) as follows:

$$\omega_n=\frac{(\beta_n L)^2}{2\pi L^2}\sqrt{\frac{1}{D_{11}^*(\rho_{eff}h)}} \tag{18}$$

In this context, $\beta_n L$ denotes the roots of the beam's characteristic equation, $\cos\beta L\cosh\beta L=1$, with a value of 4.730 for the first mode. The final formulation simultaneously incorporates the effects of mass reduction, nonlinear stiffness reduction, and all elastic couplings resulting from the layup sequence on the natural frequency.

3. Experimental procedure

3.1. Digital Image Correlation

In the present study, a random speckle pattern was created on the surface of each specimen by spraying a fine mist of black paint over a white base coat (Fig. 9a and 9b). The displacement field was then obtained by tracking this pattern in successive images. The DIC setup (Fig. 9c) consisted of a Basler avA2300-25gm camera with a 14R0011700 lens, capturing images at a frame rate of 30 Hz. Finally, the captured images were processed using GOM Correlate software to calculate and extract the full-field displacement and strain data. This powerful measurement technique forms the basis for accurately capturing material response during the static mechanical tests detailed in the following sections.

3.2. Tensile Test

Leveraging the full-field strain measurement capabilities of the DIC system described above, static tensile tests were conducted to determine the material's baseline orthotropic properties. For this purpose, six standard Type I tensile specimens were prepared in accordance with ASTM D638-14, each with a nominal thickness of 3.2 mm. The specimens were divided into two groups based on raster angle (0° and 90°), with three specimens per group. Tensile loading was conducted using a 15-ton capacity SANTAM universal testing machine at a crosshead speed of 5 mm/min. Axial elongation was measured using an extensometer, and a DIC system recorded the full-field displacement and strain (Fig. 9c and 9d). The resulting stress–strain curves and DIC data were used to calculate key mechanical properties, including elastic modulus, Poisson's ratio, ultimate tensile strength, and elongation at break for each specimen.

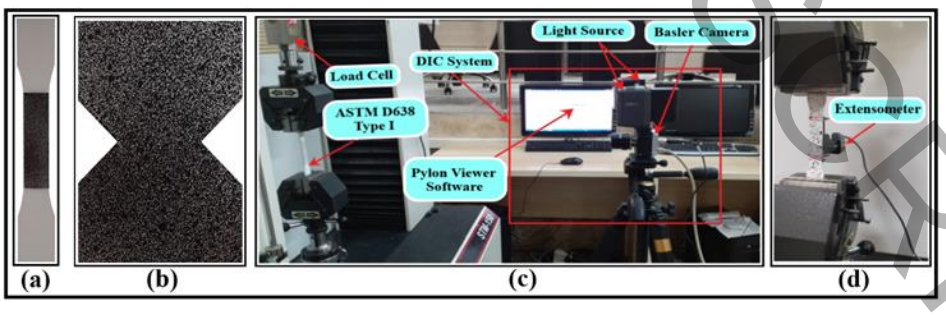


Fig. 9 DIC framework: (a, b) speckle patterns, (c, d) tensile test setups

3.3. V-Notched Rail Shear Test

The shear properties of the material were determined following the ASTM D7078 standard using three V-notched PLA specimens. A speckle pattern was applied to the specimen surface for analysis with DIC. The specimens were loaded in a shear fixture (Fig. 10a and 10b) at a rate of 2 mm/min, during which the DIC system captured the displacement and strain fields. In-plane shear strain was subsequently calculated by defining two

ACCEPTED MANUSCRIPT

virtual extensometers at ± 45° to the loading axis in the specimen's center (Fig. 10c). The resulting shear stress-strain curves were then used to determine the shear modulus and the ultimate shear strength.

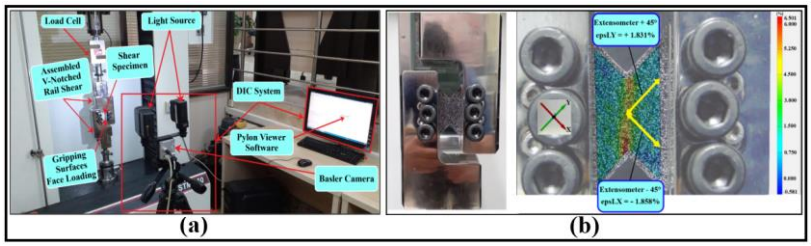


Fig. 10 Shear testing setup: (**a**) DIC optical arrangement, (**b**) fixture assembly and ± 45° virtual extensometers

3.4. Experimental modal testing

Experimental modal testing was performed on the beams using the roving hammer method to identify the components' dynamic properties, specifically their natural frequencies. The beams were suspended with soft elastic cords to approximate free-free boundary conditions (Fig. 11a). The stiffness of these cords was sufficiently low to ensure that any suspension-induced rigid-body modes remained well below the fundamental bending frequencies of the beams, thereby minimizing boundary interference. The B&K 4393 accelerometer was mounted at a fixed reference point (5 of 9 total points), and a B&K 8206 impact hammer was used to excite the structure at all nine points. To ensure repeatability and suppress measurement noise, a minimum of three valid impacts were averaged for each node, with the coherence function rigorously monitored to reject double hits and ensure high-quality FRFs. The force and acceleration signals were conditioned by a B&K 2626 charge amplifier and processed by a B&K 3560C PULSE multi-channel analyzer (Fig. 11b). The PULSE software computed the FRF from the acquired data (Fig. 11c). Finally, the FRFs were analyzed in STAR Modal software, where curve-fitting techniques were applied to extract the modal parameters, namely the natural frequencies and mode shapes (Fig. 11d).

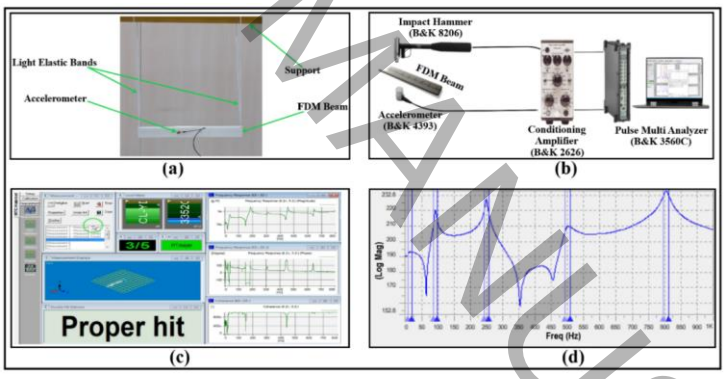


Fig. 11 Modal testing: (a) free-free suspension, (b) DAQ setup, (c) FRFs, (d) curve fitting

4. Results and Discussion

4.1. Validation Model

The porosity estimation method was evaluated using XCT images published in [14]. The superellipse-based geometric model was applied to the cross-sectional image of the sample 0° raster angle, using the same process parameters as those used to fabricate the reference specimens. The results are presented in Table 3.

Table 3 Comparison of Semi-Empirical Model and XCT Porosity Measurements

Specimen	Raster Angle (°)	Present Study (%)	Reference Study (%)	Error (%)
ASTM D638-Type IV	0	4.061	4.280	5.11
	90	4.540	4.810	5.61
	± 45°	4.670	4.875	4.20

The findings demonstrate that the proposed porosity estimation method achieves values with an average relative error of approximately 5% compared to the mean porosity measured by XCT. This minor discrepancy can be attributed to the geometric idealizations inherent in the model, which assume a uniform extruded cross-section along the raster path, whereas high-resolution XCT captures local volumetric irregularities.

ACCEPTED MANUSCRIPT

4.2. Mechanical Properties

Following the validation of the geometric porosity model, the focus shifts to quantifying the effect of these identified void fractions on the macroscopic mechanical performance, starting with the static elastic constants. The mechanical properties of the specimens, including Young's modulus, shear modulus, and Poisson's ratio at various raster angles, are summarized in Tables 4 and 5.

Table 4 Mechanical properties of standard shear test specimens

Raster Angle (°)	Specimen/Statistic	Shear Strength (MPa)	Shear Modulus (GPa)	Ultimate Shear Strain (%)
0	1	31.28	1.390	5.947
	2	30.52	1.451	7.661
	3	27.56	1.331	7.774
	Mean	29.79	1.391	7.127
	Standard Deviation	1.97	0.06	1.024

Table 5 Mechanical properties of standard tensile test specimens

Raster Angle°	Specimen/Statistic	Tensile Strength (MPa)	Poisson's Ratios	Young's Moduli (GPa)	Ultimate Tensile Strain (%)
0	1	55.58	0.373	3.790	1.742
	2	55.21	0.382	3.697	1.766
	3	51.83	0.363	3.721	1.598
	Mean	54.20	0.372	3.736	1.702
	Standard Deviation	2.070	0.010	0.048	0.091
90	1	11.83	0.244	2.480	0.503
	2	10.78	0.242	2.348	0.492
	3	10.22	0.237	2.438	0.491
	Mean	10.94	0.241	2.422	0.495
	Standard Deviation	0.820	0.004	0.067	0.007

Since fabricating a perfectly zero-porosity FDM component is practically unattainable, a baseline intrinsic Young's modulus was reverse-calculated. By substituting the experimental effective modulus from the 0° tensile tests, the SEM-extracted void volume fraction, and the calibrated exponent (m =1.35) into Eq. (6), an extrapolated baseline value of 3.803 GPa was determined for the fully fused PLA matrix. This parameter was subsequently used as a constant input in the analytical equations.

The effective engineering constants were validated against established analytical and experimental data. The comparison presented in Table 6 demonstrates strong agreement between the results.

Table 6 Comparison of elastic constants between the present model and the reference study

Property	References	Experimental Value (GPa)	Predicted Value (GPa)	Error (%)
Elastic Modulus (E_{xx})	Present Study	3.736	3.803	1.76
	Chen et al.	3.354	3.299	1.66
Elastic Modulus (E_{yy})	Present Study	2.422	2.450	1.14
	Chen et al.	2.837	2.852	0.52
Shear Modulus (G_{xy})	Present Study	1.39	1.387	0.21
	Chen et al.	1.12	1.13	0.88

The build orientation and the quality of bond strength between layers, particularly at locations where voids are likely to form, significantly influence the mechanical properties of PLA parts produced by FDM. These factors result in pronounced directional differences in elastic behavior. As shown in Fig. 12a, samples printed with a 0° raster angle achieved an average tensile strength of 54.2 MPa and an elastic modulus of 3.736 GPa. These samples display a distinct linear phase in their stress-strain response, followed by a slight curvature before experiencing sudden failure.

Full-field strain analysis using DIC, as shown in Fig. 12b, reveals an uneven strain distribution, with no dominant, continuous lines across the sample. High-strain regions, indicated by warm colors, are scattered and patchy. This distribution suggests that, despite some local inconsistencies introduced by the printing process, the voids between rasters do not serve as major stress concentrators because the applied load is aligned with the rasters, allowing the bulk material to effectively bear it.

ACCEPTED MANUSCRIPT

In contrast, setting the raster angle to 90° results in a significant reduction in ultimate strength and average elastic modulus, to 10.94 MPa and 2.422 GPa, respectively. This adjustment produces a nearly linear stress-strain response with minimal curvature until failure occurs (Fig. 12c).

The DIC contours in Fig. 12d indicate that strain bands develop along the raster direction even under low load conditions, suggesting premature strain concentration at the weak interfaces between layers. In this arrangement, voids between rasters are oriented perpendicular to the load direction and function as stress concentrators, reducing the effective cross-sectional area and leading to material failure at low strains. This decrease in effective stiffness directly causes the observed reduction in natural frequency for vibration modes associated with this orientation.

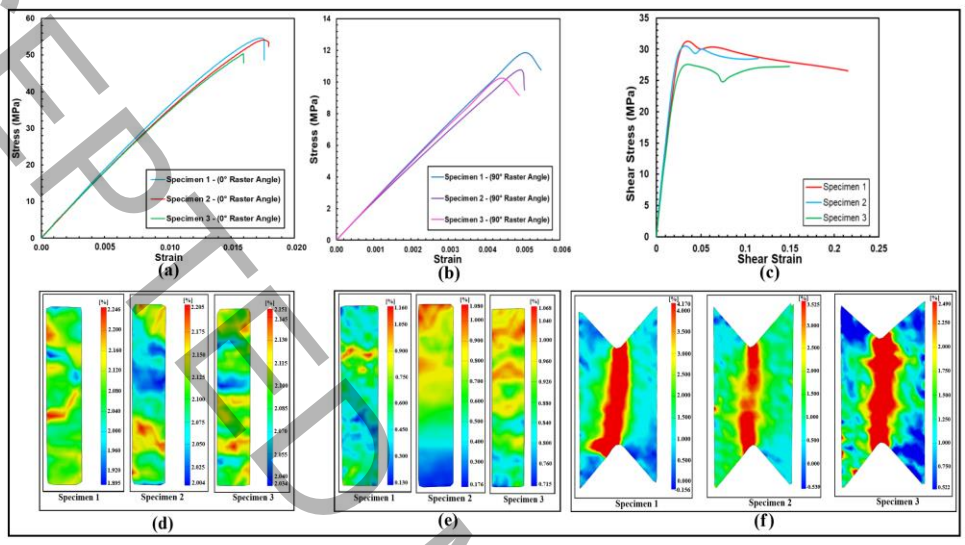


Fig. 12 Stress-strain curves and corresponding DIC strain fields for: **(a, d)** 0° raster angle, **(b, e)** 90° raster angle, and **(c, f)** ASTM D7078 in-plane shear specimens

Fig. 12e presents the DIC shear stress-strain curves, which exhibit pronounced nonlinear behavior. Fig. 12f illustrates a significant concentration of strain within the sample's central gauge section. The jagged and irregular boundaries of the high-strain shear band, indicated by the red area, result from voids and defects in the bonds between printed lines. These defects establish a path of least resistance, thereby facilitating inter-raster slip. The observed strain concentration indicates that voids not only reduce static strength but also disrupt structural continuity, thereby substantially influencing the structure's dynamic response.

4.3. Parametric analysis of the effect of porosity

The parametric analysis presented in Fig. 13(a–c) reveals that the degradation of elastic properties with increasing porosity does not follow a uniform trend. While all engineering constants decrease, the rate of this reduction varies significantly depending on the loading mode. The longitudinal Young's modulus exhibits a moderate decline, following the power-law relationship (Eq. (6)). In contrast, the shear and transverse moduli display a much higher sensitivity to porosity levels. This disparity suggests that inter-raster voids disproportionately impair shear load transfer mechanisms and transverse bonding efficiency.

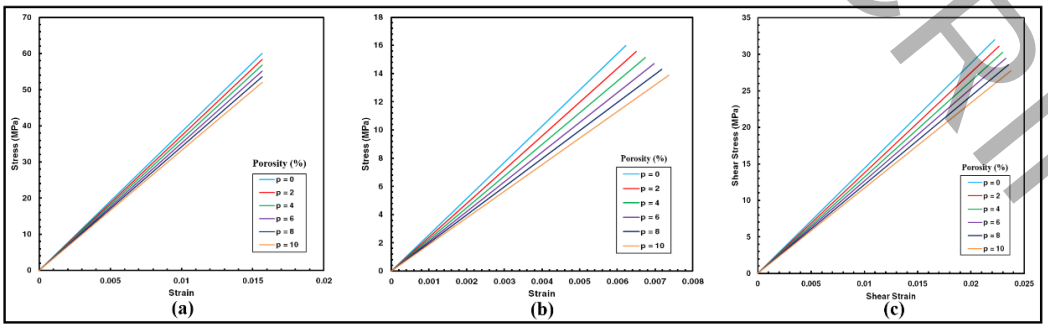


Fig. 13 Porosity effect on moduli: (**a**) 0° tensile, (**b**) 90° tensile, and (**c**) 0° shear

ACCEPTED MANUSCRIPT

4.4. Dynamical Characterization

While the static analysis highlights the degradation of stiffness due to porosity, a complete structural assessment requires examining the vibratory response. Therefore, this section extends the investigation to the dynamic domain, validating the analytical model against experimental modal tests.

To validate the proposed framework, an initial benchmark study was conducted using a non-porous ($p = 0$) 8-layer unidirectional Carbon/Epoxy beam (250×25×2.2 mm), as detailed in the literature [22] As demonstrated in Table 7, the calculated natural frequencies show good agreement with the FSDT-based reference values for both clamped-clamped (C-C) and simply supported (S-S) boundary conditions.

Table 7 Comparison of natural frequencies between present study and the reference study

BCs	Mode Number	Frequency Parameter ($\beta_n L$)	Present Study (Hz)	Exp (Reference Study) (Hz)	FEA (Reference Study) (Hz)	Error (%)
C-C	1	4.730	178.86	185.00	185.14	3.40
	2	7.853	493.04	510.00	509.44	3.21
	3	10.99	966.56	956.25	958.85	0.80
S-S	1	3.141	78.902	78.750	80.72	2.25
	2	6.283	315.60	327.50	323.19	2.34
	3	9.424	710.12	701.25	705.37	0.67

Table 8 summarizes the results from both the analytical model and experimental modal tests for beams with different raster angles, all tested under free-free boundary conditions. Natural frequencies were determined using the Circle Fit method applied to the Frequency Response Functions (FRFs) presented in Fig. 14. Additionally, the influence of porosity on the dynamic response of FDM-printed beams is examined in this study.

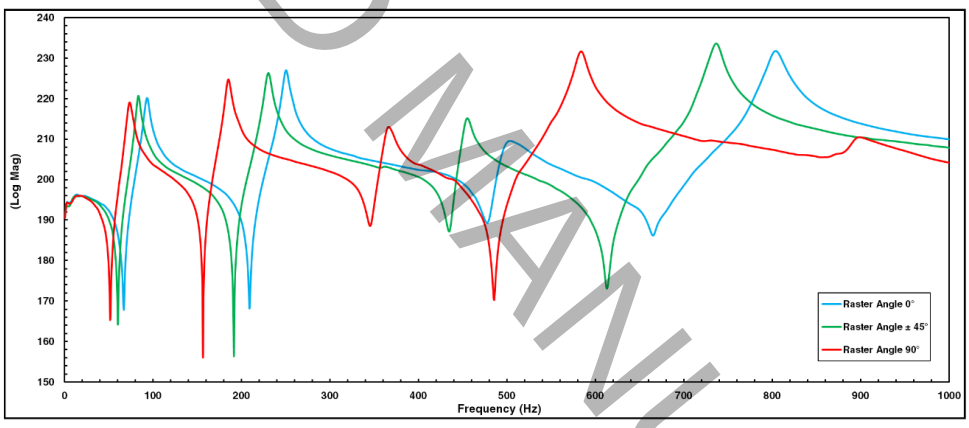


Fig. 14. Frequency response functions for beams with various raster angles

Table 8 Comparison between experimental and analytical natural frequencies of FDM beams

Raster Angle°	Mode Number	Experimental Natural Frequency (Hz)	Analytical Natural Frequency (Hz)	Error (%)
0	1	92.664	91.498	1.27
	2	250.18	252.21	0.80
	3	497.39	494.44	0.59
	4	804.23	817.35	1.60
90	1	73.043	72.413	0.87
	2	184.67	199.61	7.48
	3	364.26	391.31	6.91
	4	584.39	646.86	9.65
± 45	1	83.083	90.456	8.15
	2	229.90	249.34	7.79
	3	454.28	488.81	7.06
	4	737.04	808.04	8.78

The results validate the porosity-based analytical model, though discrepancies arise from idealizations, such as perfect interlayer bonding and uniform void geometry, and from experimental deviations, such as the elastic support stiffness. These factors overlook inherent defects that reduce the actual stiffness, leading the model to overestimate the natural frequencies slightly.

ACCEPTED MANUSCRIPT

4.5. Effect of Porosity on Dynamic Response

In this section, the effect of porosity on the mass, stiffness, and natural frequencies of the beams is investigated (Figs. 15a–d). The analytical and experimental results indicate a direct relationship between increased porosity and variations in the structure's dynamic behavior.

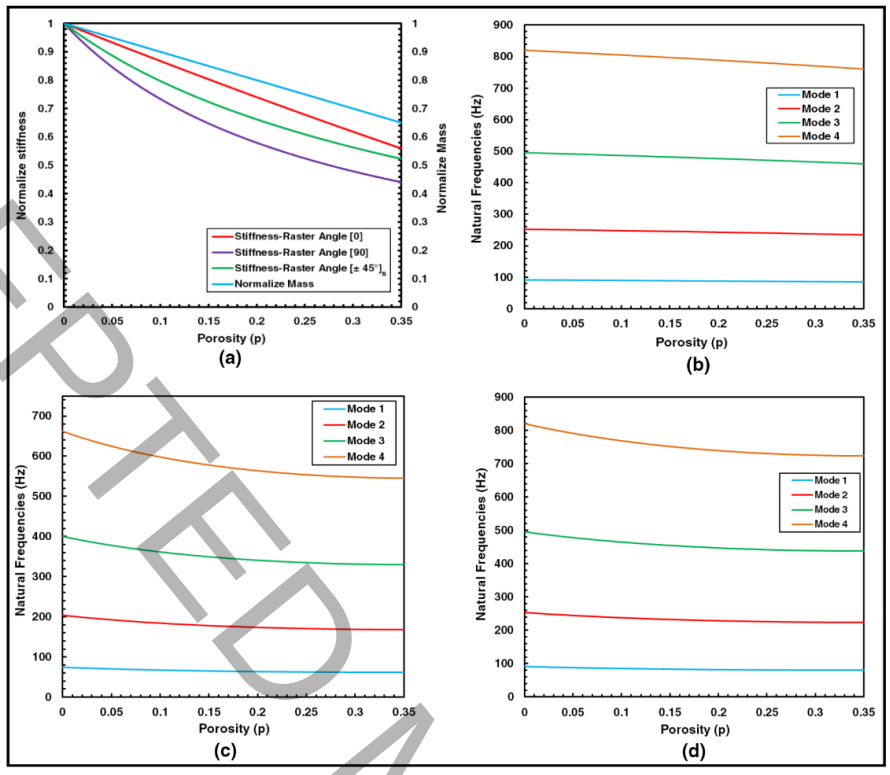


Fig. 15 Effect of porosity on: (**a**) effective stiffness and mass; (**b–d**) natural frequencies for raster angles

In Fig. 15a, the effect of porosity on the vibrational behavior of beams is quantified by normalizing the effective mass and effective bending stiffness relative to the non-porosity state. The results indicate that the normalized mass decreases linearly with increasing porosity, whereas the bending stiffness declines more steeply. This behavior varies with raster angle; the 0° raster angle retains the highest relative stiffness, while the 90° and ± 45 ° orientations show more severe reductions. This disparity in the reduction rates of mass and stiffness is the primary driver of variations in natural frequencies. Consequently, given that natural frequency is proportional to the square root of the stiffness-to-mass ratio, the more rapid decline in stiffness compared to mass results in an overall reduction in natural frequencies.

Figs. 15b–d illustrate the variation of natural frequencies (modes 1 to 4) as a function of porosity for raster angles of 0°, 90°, and ± 45°. For all vibration modes and raster angles, natural frequencies decrease with increasing porosity. The highest natural frequencies are observed for the 0° raster angle (Fig. 15b), attributed to the alignment of rasters with the beam's longitudinal axis and the resulting higher flexural stiffness. Conversely, the lowest frequencies occur at the 90° raster angle (Fig. 15c), where structural strength relies primarily on inter-raster and inter-layer bonding rather than the strength of the rasters themselves.

Porosity in FDM is a critical factor influencing the mechanical and dynamical behavior of fabricated structures. Failure to account for porosity can lead to substantial computational errors when estimating dynamic characteristics. The reduction in natural frequencies due to porosity lowers the resonance threshold, increasing the risk that low-frequency operational vibrations may induce catastrophic failures. Consequently, it is essential to account for voids and their detrimental effects during the FDM process.

5. Conclusion

This study addressed the critical need for a quantitative link between FDM microstructure and macroscopic dynamic performance. Through a combined analytical and experimental investigation, the following conclusions are drawn:

ACCEPTED MANUSCRIPT

- **Enhanced Geometric Accuracy:** Integrating the Superellipse function with actual toolpath data yielded superior results compared to conventional circular models. By accurately reconstructing the flattened geometry of inter-raster voids, this method minimized estimation errors, providing a robust basis for mechanical prediction.
- **Anisotropy and Failure Mechanisms:** Experimental characterization confirmed a pronounced anisotropy in mechanical behavior. While the 0° raster angle exhibited optimal load-bearing capacity, the 90° raster angle demonstrated significant vulnerability. DIC analysis revealed that this weakness stems from premature strain localization at the void interfaces, indicating that inter-layer bonding is the structural bottleneck.
- **Porosity as a Dynamic Parameter:** The study found that porosity fundamentally alters the vibrational signatures of components. A key finding is the non-uniform sensitivity of natural frequencies to void content; specifically, the 90° raster angle suffers a substantial frequency drop due to a stiffness degradation rate that outpaces mass reduction. This highlights the risk of unexpected resonance in transversely loaded FDM parts.
- **Framework Validation:** The fact that the proposed porosity-inclusive CLT model shows a strong correlation with the experimental modal results (mean error ≈ 5%) shows that the framework can be regarded as a robust predictive tool.
- **Future Outlook:** Future research should extend this semi-empirical approach to a broader range of polymeric materials to test generalizability. Furthermore, integrating this void model into large-scale Finite Element simulations could enable the precise dynamic analysis of complex, industrially relevant FDM geometries under variable printing parameters.

Despite the successful demonstration of the proposed hybrid framework, several limitations and contextual boundaries must be acknowledged. First, the empirical calibration of the stiffness-reduction exponent (m) relied on a specific sample set with a narrow porosity range (1.3–1.9%) characteristic of high-density structural parts. This inherently limits the current predictive universality; independent blind validations using broader datasets and wider porosity levels are required in future work to avoid circular dependencies and verify the model for highly porous structures. Second, the current study is restricted to PLA processed under a single set of printing parameters, and extending this framework to diverse thermoplastic materials and complex multi-parameter interactions remains an essential direction for subsequent research. Finally, rather than acting as a universal replacement for industrial XCT systems, the proposed G-code-based workflow functions as an efficient, targeted predictive tool for volumetric scanning, providing a practical pathway for the targeted design and optimization of additively manufactured structures.

References

[1] V. Cojocaru, D. Frunzaverde, C.-O. Miclosina, G. Marginean, The Influence of the Process Parameters on the Mechanical Properties of PLA Specimens Produced by Fused Filament Fabrication—A Review, in: Polymers, 2022, pp. 886.

[2] H.I. Medellin-Castillo, J. Zaragoza-Siqueiros, Design and Manufacturing Strategies for Fused Deposition Modelling in Additive Manufacturing: A Review, Chinese Journal of Mechanical Engineering, 32(1) (2019) 53.

[3] M. Moradi, R. Hashemi, A. Hosseinzadeh, M. Kasaeian-Naeini, Influence of infill settings on the flexural properties of 3D printed ABS plus polymer parts in bending loading, AUT Journal of Mechanical Engineering, 9(1) (2025) 83–96.

ACCEPTED MANUSCRIPT

[4] V. Fartashvand, A. Kami, A. Bagheri, Enhancing Mechanical Properties of Ultrasonically-Treated 3D-Printed Acrylonitrile Butadiene-Styrene and Polylactic Acid Parts: A Full Factoria, AUT Journal of Mechanical Engineering, 7(3) (2023) 283–296.

[5] Y. Tao, F. Kong, Z. Li, J. Zhang, X. Zhao, Q. Yin, D. Xing, P. Li, A review on voids of 3D printed parts by fused filament fabrication, Journal of Materials Research and Technology, 15 (2021) 4860–4879.

[6] S. Cerda-Avila, H. Medellín-Castillo, T. Lim, Analytical models to estimate the structural behaviour of fused deposition modelling components, Rapid Prototyping Journal, 27 (2021) 658–670.

[7] A. Garg, A. Bhattacharya, An insight to the failure of FDM parts under tensile loading: finite element analysis and experimental study, International Journal of Mechanical Sciences, 120 (2017) 225–236.

[8] L. Li, Q. Sun, C. Bellehumeur, P. Gu, Composite Modeling and Analysis for Fabrication of FDM Prototypes with Locally Controlled Properties, Journal of Manufacturing Processes, 4(2) (2002) 129–141.

[9] C. Casavola, A. Cazzato, V. Moramarco, C. Pappalettere, Orthotropic mechanical properties of fused deposition modelling parts described by classical laminate theory, Materials & Design, 90 (2016) 453–458.

[10] J.F. Rodríguez, J.P. Thomas, J.E. Renaud, Mechanical behavior of acrylonitrile butadiene styrene fused deposition materials modeling, Rapid Prototyping Journal, 9(4) (2003) 219–230.

[11] E. Polyzos, S.B. Ravindranath, D.V. Hemelrijck, L. Pyl, Analytical and numerical modeling of voids in additively manufactured thermoplastic parts, Additive Manufacturing, 48 (2021) 102356.

[12] R. Chen, A.F. Kaplan, D.G. Senesky, Closed-form orthotropic constitutive model for aligned square array mesostructure, Additive Manufacturing, 36 (2020) 101463.

[13] S. Sommacal, A. Matschinski, K. Drechsler, P. Compston, Characterisation of void and fiber distribution in 3D printed carbon-fiber/PEEK using X-ray computed tomography, Composites Part A: Applied Science and Manufacturing, 149 (2021) 106487.

[14] X. Wang, L. Zhao, J.Y. Fuh, H.P. Lee, Effect of Porosity on Mechanical Properties of 3D Printed Polymers: Experiments and Micromechanical Modeling Based on X-ray Computed Tomography Analysis, in: Polymers, 2019, pp. 1154.

[15] T. Yao, H. Ouyang, S. Dai, Z. Deng, K. Zhang, Effects of manufacturing micro-structure on vibration of FFF 3D printing plates: Material characterisation, numerical analysis and experimental study, Composite Structures, 268 (2021) 113970.

[16] V.E. Kuznetsov, A.N. Solonin, O.D. Urzhumtsev, R. Schilling, A.G. Tavitov, Strength of PLA Components Fabricated with Fused Deposition Technology Using a Desktop 3D Printer as a Function of Geometrical Parameters of the Process, in: Polymers, 2018, pp. 313.

[17] J.A. Choren, S.M. Heinrich, M.B. Silver-Thorn, Young's modulus and volume porosity relationships for additive manufacturing applications, Journal of Materials Science, 48(15) (2013) 5103–5112.

[18] R. Chen, D.G. Senesky, A closed-form orthotropic constitutive model for fused filament fabrication materials.

[19] D.S. Sharma, Stresses around hypotrochoidal hole in infinite isotropic plate, International Journal of Mechanical Sciences, 105 (2016) 32–40.

[20] K.R.Y. Simha, S.S. Mohapatra, Stress concentration around irregular holes using complex variable method, Sadhana, 23(4) (1998) 393–412.

[21] S. Rao, Vibration of Continuous Systems, 2019.

[22] P. Das, S. Sahu, Free vibration analysis of industry-driven woven fiber laminated carbon/epoxy composite beams by experimental and numerical approach, Polymers and Polymer Composites, 29 (2021) S1371–S1385.

ACCEPTED MANUSCRIPT